Effects of surface potentials on Goos-Hänchen and Imbert-Fedorov shifts in Weyl semimetals

Ninad Kailas Dongre [1] and Krishanu Roychowdhury [2,3]
[1]*Department of Physics, The University of Texas at Dallas, Richardson, Texas 75080, USA*
[2]*Department of Physics, Stockholm University, SE-106 91 Stockholm, Sweden*
[3]*Max-Planck-Institut für Physik komplexer Systeme, Nöthnitzer Strasse 38, 01187 Dresden, Germany*

(Received 8 June 2021; revised 2 August 2022; accepted 9 August 2022; published 17 August 2022)

Weyl semimetals exhibit a myriad of exotic transport responses, among which, the Goos-Hänchen (GH) and Imbert-Fedorov (IF) effects have recently garnered substantial attention. Besides the usual parametric dependence inherited from the underlying Hamiltonian to describe a Weyl system, the IF shift particularly carries a topological identity—it depends on the chirality of the Weyl cones. Observing such signatures following the trail of theoretical predictions applied to clean systems can be severely obfuscated by surface potentials induced by localized impurities that are naturally present in real materials hosting the semimetallic phase. Classifying these potentials, we study their effects on GH and IF shifts to provide useful guidance to experiments that are tuned to the objective of characterizing Weyl semimetals and leveraging them to provide the basis for future technological advances. A transfer matrix-based approach is proposed to study the profile of Weyl wave functions scattering from the impurity potentials. As we unfold, the presence of such potentials can lead to several remarkable effects such as the complete nullification of the IF shift and valley inversion.

DOI: 10.1103/PhysRevB.106.075414

I. INTRODUCTION

The Goos-Hänchen [1–3] (GH) and Imbert-Fedorov [4–6] (IF) shifts, first discovered in the context of wave optics, have now enjoyed wide application in a variety of systems [7–21] that includes optical waveguides, metamaterials, plasmonics, and quantum systems. These effects transpire for beams of finite width (i.e., a distributed spectrum of plane waves) whose reflection and refraction do not quite follow the simple geometric rules of Newtonian optics—they feature lateral and angular shifts with respect to the point of incidence that admit a geometrical description [22] instead. For instance, when a traveling photon beam suffers multiple total internal reflections inside an optical waveguide, a measurable GH shift along the direction of propagation is observed which can be attributed to a finite penetration of the evanescent beam into the cladding material at each turn. This is reminiscent of the tunneling of quantum particles through finite barriers owing to their dual (wave-particle) nature and has inspired researchers to explore such scattering effects in various quantum systems such as two-dimensional electron gas (2DEG) nanostructures [23–25] and Dirac materials like graphene [19,26–35] and transition metal dichalcogenides [36], enabling new device applications that extend, as well, to a terahertz regime [37–39]. The GH shift, occurring in a system of 2DEG subject to a tunable electric potential and hosted between magnetic stripes, has been utilized to construct an efficient spin beam splitter [23,40]. While spin manipulation of such type is highly desirable for spintronics and quantum information applications, the valley degrees of freedom in electronic systems (such as semiconductors and semimetals) are also of concurrent and intensive interest [28,41], especially for rapidly emerging quantum technologies like valleytronics.

On both fronts, Dirac materials have been at the center stage over the last few decades. Graphene (along with other materials of similar band structures) has emerged as a paradigmatic model wherein a host of exotic electronic phenomena that arises in two dimensions has been proposed and verified in experiments (see Ref. [42] for a review). The GH shift for the massless electrons in graphene manifests as a pseudospin-dependent scattering effect that results in a quantized jump in the conductance of heterojunctions [19]. In the same system, a valley-dependent GH shift is studied by means of tailoring the local strain profile [41] exhibiting a close resemblance to the spin manipulation in Ref. [23] and also, in part, to the aforementioned optical and electronic analogs.

The IF effect, likewise, has also been explored in graphene systems [43–49], and recently, to some extent, in Weyl semimetals [50–56] which serve as the model of the present study. Weyl semimetals are characterized by topologically robust nodes (immune to arbitrary perturbations) in the bulk and Fermi arc surface states [57]. The nodes are of distinct chirality, referred to as Weyl cones (singly degenerate, as opposed to the doubly degenerate Dirac cones in, e.g., graphene), and responsible for strange phenomena like *chiral anomaly*, exclusive in three dimensions. Aside from the bulk nodes, the surface states are also a distinctive hallmark of these

topological semimetals which have been experimentally probed (such as in TaAs or NbAs) and bear important implications for various transport properties of these systems (see Ref. [58] and references therein). The beam shifts can be exploited to probe the separation of these Weyl nodes in momentum space [54], and particularly, the IF shift being a topological effect (depends on the chirality of the nodes), provides a measure of Berry curvature [50]. Thus, the factors that can potentially influence these measurements should be thoroughly examined for a precise characterization of the underlying system which underpins the present study.

While previous studies on the shifts in Weyl semimetals have focused only on pristine surfaces, real materials would naturally host impurities that give rise to localized surface potentials of various kinds, akin to a scenario in topological insulators [59–61]. In topological insulators, the surface potentials that respect time-reversal symmetry are capable of influencing surface spin texture, shifting the Dirac points, and eliminating blockades imposed by orbital orthogonalities across heterojunctions. In Weyl systems, these potentials could break time-reversal or inversion (or none), which is anyway required to stabilize a Weyl semimetallic phase in the bulk. For instance, magnetic impurities can populate the surface of a magnetic Weyl semimetal such as $Co_3Sn_2S_2$ [62] while spin-orbit type impurities can be found in inversion breaking Weyl semimetals such as candidates from the TaAs material class [63]. Apart from bulk impurities, these potentials are also of great relevance to experiments dedicated to probing surface transport (such as conductivities) in these topological materials and also towards validating the theoretical predictions based on clean surfaces and derived from the bulk-boundary correspondence.

Among many intriguing consequences, localized bulk impurities in Weyl semimetals can lead to suppression in the nodal density of states which may or may not be lifted by impurity-induced resonances [64]. Besides, these impurities also exhibit prominent features for the surface states such as giving rise to bound states for certain parameter values in the Hamiltonian that lead to distinct topological phases [65]. As the lateral shifts concerned are exclusively surface phenomena and such shifts, particularly for a Weyl semimetal surface, are intricately related to the Fermi arc structure [55], we naturally ask to what extent are they influenced by the presence of impurity-induced surface potentials that are compatible with the symmetry breaking in the bulk.

In this paper we model the impurity as planelike infinite-amplitude potential lying on an infinite surface which can be solved using a transfer-matrix (T-matrix) based approach [66]. The resultant potential enables a nontrivial T matrix to affect the wave function continuity in the vicinity of the surface which causes the concerned beam shifts susceptible to the perturbations. An advantage of using this formalism is that the shift can be traced for arbitrary strengths of the impurity potential. Since topological materials are primarily characterized by their surface signatures, it is legitimate to assess the robustness of these signatures against such potentials. The key findings of this paper entail a thorough analysis of GH and IF shifts in the presence of such imperfections. In distinction to the results obtained from the hitherto studied clean surfaces, our work reveals that certain types of potentials can abate the topological effects and also give rise to phenomena like valley inversion.

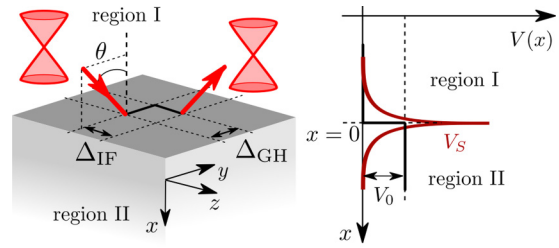

FIG. 1. The schematic of the Weyl semimetal surface hosting surface potential V_S at $x = 0$ with the two lateral shifts indicated. The plane of incidence is the x-y plane such that the in-plane lateral shift (GH shift) is along the y axis and the out-of-plane shift (IF shift) is along the z axis. The barrier potential to distinguish the two regions I and II is denoted by V_0.

The remainder of the article is structured as follows. In Sec. II we introduce the model and review some aspects of the GH and the IF shift for a clean surface. In Sec. III we discuss the transfer matrix-based approach that applies to analyze the Weyl wave function across an interface hosting impurity-induced surface potentials. These potentials are classified in Sec. IV where the shift calculations are revisited for each of the classes. We summarize the results in Sec. V and discuss future work.

II. GH AND IF SHIFTS FOR A CLEAN INTERFACE

We start by reviewing the results from a previous work that computed the GH and the IF shifts for a clean interface [50]. For calculations we consider the surface (or interface) to be the y-z plane at $x = 0$ which breaks the translation symmetry along x but retains along the other two directions (see Fig. 1), however, the formulation presented in this article, as well, applies to surfaces of other orientations.

The Hamiltonian of the system is described by

$$H = \begin{cases} H_{\rm I} = \chi \hbar v_F k_i \sigma_i, & x \leqslant 0, \\ H_{\rm II} = \chi \hbar v_F k_i \sigma_i + V_0, & x > 0, \end{cases} \tag{1}$$

where $i \in \{x, y, z\}$ and χ ($\chi = \pm 1$) denotes the chirality of the Weyl cones. We refer to the region $x \leqslant 0$ as region I, and the region $x > 0$ as region II as in Fig. 1. These two regions are distinguished by applying a chemical potential difference V_0 between them which creates a finite barrier for the Weyl fermions to scatter off. Furthermore, v_F denotes the Fermi velocity, which is taken the same on both sides, and σ_i are the Pauli matrices representing the pseudospin degrees of freedom. Throughout the calculations that follow, we adopt the units in which $\hbar = v_F = 1$, however, while presenting the final expressions of the shifts, the factor of $\hbar v_F$ is duly restored.

A beam of Weyl fermions, in the form of a Gaussian wave packet, incident on the interface at $x = 0$ is modeled by

$$\Psi^{\rm in}(\mathbf{r}) = \int_{-\infty}^{\infty} dk_y dk_z \; f(k_y, k_z) \psi^{\rm in}(\mathbf{k}, \mathbf{r}), \tag{2}$$

where the Gaussian function f is assumed to be localized around $(\bar{k}_y, \bar{k}_z)$ as

$$f(k_y, k_z) = \frac{1}{2\pi\sqrt{\Delta_y \Delta_z}} \exp\left[-\frac{(k_y-\bar{k}_y)^2}{2\Delta_y^2} - \frac{(k_z-\bar{k}_z)^2}{2\Delta_z^2}\right], \tag{3}$$

Δ_y (Δ_z) denoting the width of the wave packet along y (z). The spinor part of the incident wave function ψ^{in} satisfies the Schrödinger equation $H_{\text{I}}\psi^{\text{in}} = E\psi^{\text{in}}$, and including the plane wave phase factor $e^{i\mathbf{k}\cdot\mathbf{r}}$,

$$\psi^{\text{in}}(\mathbf{k}, \mathbf{r}) = C_i \begin{bmatrix} 2\eta\chi e^{-i\theta/2} \\ \tilde{\eta} e^{i\theta/2} \end{bmatrix} e^{i\mathbf{k}\cdot\mathbf{r}}, \tag{4}$$

where $k_x = \sqrt{E^2 - k_y^2 - k_z^2}$, $\tan\theta = k_y/k_x$, $\eta = \sqrt{\frac{E-k_z}{E+k_z}}$, $\tilde{\eta} = \eta^2(1+\chi) + (1-\chi)$, and C_i is the normalization constant. Taking the plane of incidence to be the x-y plane, θ represents the angle of incidence for the incident beam measured from the surface normal perpendicular to the y-z plane at the point of incidence (see Fig. 1).

The reflected wave packet can be expressed in a similar form as the incident one. Multiplied by the reflection coefficient $r = |r|e^{i\phi_r}$, it is

$$\Psi^{\text{re}}(\mathbf{r}) = \int_{-\infty}^{\infty} dk_y dk_z \; f(k_y, k_z)\, r\psi^{\text{re}}(\mathbf{k}, \mathbf{r}), \tag{5}$$

where ϕ_r is the reflection phase and $\psi^{\text{re}}(\mathbf{k}, \mathbf{r})$ is obtained from $\psi^{\text{in}}(\mathbf{k}, \mathbf{r})$ in Eq. (4) via $k_x \to -k_x, \theta \to \pi - \theta$. For the phenomena concerned, we will be considering total reflection from the interface in the region I with $|r| = 1$, and for this, the mode on the other side (region II) must be evanescent. Note this happens only for values of the incident angle θ greater than a critical value θ_c which, as will be shown later, depends on the ratio of the barrier height to the incident energy V_0/E.

Linearizing the phases θ and ϕ_r in terms of $\bar{k}_y$ and $\bar{k}_z$, the integrals in Eqs. (2) and (5) provide the centers of the incident and the reflected wave packets, respectively, from which the (spinor) component-wise spatial shifts along y and z follow as

$$\begin{aligned} \Delta_{\pm}^{y} &= -\frac{\partial}{\partial k_y}\phi_r(\bar{k}_y, \bar{k}_z) \mp \frac{\partial}{\partial k_y}\theta(\bar{k}_y, \bar{k}_z), \\ \Delta_{\pm}^{z} &= -\frac{\partial}{\partial k_z}\phi_r(\bar{k}_y, \bar{k}_z) \mp \frac{\partial}{\partial k_z}\theta(\bar{k}_y, \bar{k}_z), \end{aligned} \tag{6}$$

where $\pm$ refers to the shifts of the two spinor components. The full spatial shifts are then given as the weighted average of the individual shifts for each of the spinor components,

$$\Delta^{y(z)} = \frac{4\eta^2\Delta_+^{y(z)} + \tilde{\eta}^2\Delta_-^{y(z)}}{4\eta^2 + \tilde{\eta}^2}. \tag{7}$$

As the results do not depend on the shape of the wave packets, we conveniently adopt a reference by setting $\bar{k}_z = 0$ which aligns the GH and the IF shift along y and z axis, respectively, and thus simplifies Eq. (7) to

$$\begin{aligned} \Delta_{\text{GH}} \equiv \Delta^{y} &= \frac{4\eta^2\Delta_+^{y} + \tilde{\eta}^2\Delta_-^{y}}{4\eta^2\chi^2 + \tilde{\eta}^2} = -\frac{\partial\phi_r}{\partial k_y}, \\ \Delta_{\text{IF}} \equiv \Delta^{z} &= \frac{4\eta^2\Delta_+^{z} + \tilde{\eta}^2\Delta_-^{z}}{4\eta^2\chi^2 + \tilde{\eta}^2} = -\frac{\partial\phi_r}{\partial k_z}. \end{aligned} \tag{8}$$

To quantify the shifts, it then remains to compute the reflection phase ϕ_r using the continuity of the wave functions at the interface

$$\psi^{\text{tr}}(\mathbf{k}, 0) = \psi^{\text{in}}(\mathbf{k}, 0) + \psi^{\text{re}}(\mathbf{k}, 0), \tag{9}$$

where the transmitted spinor $\psi^{\text{tr}}(\mathbf{k}, \mathbf{r})$ in region II has an evanescent form at energy E as

$$\psi^{\text{tr}}(\mathbf{k}, \mathbf{r}) = C_t \begin{bmatrix} -i \\ \beta_\chi \end{bmatrix} e^{-\kappa x} e^{i(k_y y + k_z z)}; \quad \beta_\chi = \frac{k_y + \kappa}{k_z + \chi(E - V_0)}, \tag{10}$$

C_t being the normalization constant and $\kappa = \sqrt{k_z^2 + k_y^2 - (E-V_0)^2} > 0$ setting the inverse decay length. Equation (9) yields a chirality-dependent reflection phase

$$\phi_r = -\theta - \frac{\pi}{2} + 2\tan^{-1}\left[\frac{\tilde{\eta}\cos\theta}{2\eta\chi\beta_\chi - \tilde{\eta}\sin\theta}\right], \tag{11}$$

from which the spatial shifts follow as

$$\Delta_{\text{GH}} = \frac{\hbar v_F\left(1 + \sin^2\bar{\theta} - \frac{V_0}{E}\right)}{\kappa \sin\bar{\theta}\cos\bar{\theta}}; \quad \Delta_{\text{IF}} = -\frac{\hbar v_F \chi}{E\tan\bar{\theta}}, \tag{12}$$

where $\tan\bar{\theta} = \bar{k}_y/\bar{k}_x$. The critical angle to ensure a total reflection from the interface is given by $\theta_c = \sin^{-1}|V_0/E - 1|$.

Note the GH shift on a clean surface is not a chirality-dependent phenomenon while the IF shift is and can be interpreted as a topological effect [50]. This is attributed to the fact that during the reflection the Weyl fermions retain their valley characteristics due to momentum conservation on the surface which is in sharp distinction with the optical analog where the polarization of the photons does get altered during reflection. We further note that the IF shift is independent of the ratio of the barrier height to the incident energy V_0/E. The GH shift, on the other hand, changes sign at a given angle of incidence $\theta^* = \sin^{-1}\sqrt{\sin\theta_c}$—it is negative for $\theta_c < \bar{\theta} < \theta^*$ while positive for $\theta^* < \bar{\theta}$ irrespective of the values of V_0/E, and likewise for $\bar{\theta} \to -\bar{\theta}$.

So far we have discussed the shifts for a clean interface. In the following sections we will demonstrate how they are modified when the same interface harbors different types of impurity-induced surface potentials that affect the continuity equation stated above and the resultant reflection phase. In fact, in the presence of certain types of surface potentials, the shifts feature distinct asymmetry between the valleys resembling the effects of intervalley scattering [52].

III. THE TRANSFER MATRIX APPROACH

For Weyl (or Dirac) fermions subject to a delta potential scattering, the transfer matrix accounts for the rotation between the spinors on the two sides of the potential [67]. This approach is adopted extensively in transport calculations to compute observables like surface conductance, Aharonov-Bohm oscillations, and spin Berry phase in various mesoscopic systems including topological insulators with impurities [68–70].

The spatial profile of the full Hamiltonian in the presence of a delta function-type surface potential $V_S(x) = \mathcal{V}\delta(x)$ is given by

$$\mathcal{H} = \chi(\sigma_a k_a - i\sigma_x\partial_x) + V_0\Theta(x) + \mathcal{V}\delta(x), \tag{13}$$

where $a \in \{y, z\}$ as $k_{y,z}$ are regarded as good quantum numbers for we have imposed periodic boundary conditions on the interface; $\mathcal{V}$ denotes the surface potential (see Fig. 1) which could be a scalar or a spin-valued operator. The Schrödinger equation $\mathcal{H}\psi = E\psi$ can be recast as $\partial_x\psi = \mathcal{H}_0(x)\psi$ leading to a path-ordered solution of $\psi(x)$ as $\psi(x_2) = \mathcal{T}_{x_2,x_1}\psi(x_1)$ where the transfer matrix $\mathcal{T} = \mathcal{P}_x \exp[\int_{x_1}^{x_2} dx\, \mathcal{H}_0(x)]$, $\mathcal{P}_x$ denoting the path ordering [70]. For the interface at $x = 0$ (see Fig. 1), the transfer matrix pertinent to the model in Eq. (13) turns out to be

$$\mathcal{T} = \lim_{\epsilon\to 0} \mathcal{P}_x \exp\left[-i \int_{-\epsilon}^{+\epsilon} dx\, \sigma_x V_S(x)\right] = e^{-i\sigma_x \mathcal{V}}. \tag{14}$$

The continuity equation in Eq. (9) gets modified to

$$\psi^{\rm tr}(\mathbf{k}, 0^+) = \mathcal{T}[\psi^{\rm in}(\mathbf{k}, 0^-) + \psi^{\rm re}(\mathbf{k}, 0^-)], \tag{15}$$

and so does the reflection phase ϕ_r accordingly. This is how the spatial shifts are expected to get modified in the presence of various surface potentials.

IV. SURFACE POTENTIALS

In this section we will consider a family of surface potentials by expressing the surface term $\mathcal{V}$ in Eq. (13) as

$$\mathcal{V} = \lambda + \mathbf{V}\cdot\sigma, \tag{16}$$

where λ is a real constant, and the components of the vector $\mathbf{V} = (V_x, V_y, V_z)$ are, in general, real functions of k_y and k_z. In particular, we take note of the following cases:

(i) Scalar potential: $\lambda \neq 0$, $\mathbf{V} = 0$.

(ii) Magnetic potential: Uniform magnetic field specified by $V_x = B_x$, $V_y = B_y$, $V_z = B_z$ where $B_{x,y,z}$ are constants and $\lambda = 0$.

(iii) Spin-orbit potential of Rashba type: $\lambda = V_x = 0$, but V_y and V_z are linear functions of k_y and k_z as $V_y = -\alpha_R k_z$ and $V_z = \alpha_R k_y$.

(iv) Spin-orbit potential of Dresselhaus type: $\lambda = V_x = 0$, but V_y and V_z are linear functions of k_y and k_z as $V_y = \alpha_D k_y$ and $V_z = -\alpha_D k_z$.

In the following subsections we compute the GH and the IF shift from the resultant ϕ_r while addressing the above four cases separately. It should, however, be noted that combinations of them are also likely to occur on the surface of a Weyl semimetal. We will illustrate one such combination in which the surface potential includes both scalar and magnetic impurities.

A. Scalar potential

For a scalar surface potential of the form $V_S = \lambda\delta(x)$, the transfer matrix that connects the two spinors across the interface is $\mathcal{T} = e^{-i\sigma_x\lambda}$ which results in a chirality-dependent reflection phase

$$\phi_r = -\theta - \frac{\pi}{2} + 2\tan^{-1}\zeta,$$

where

$$\zeta = \frac{\tilde{\eta}\cos\theta(1 - \beta_\chi \tan\lambda)}{2\eta\chi(\tan\lambda + \beta_\chi) - \tilde{\eta}\sin\theta(1 - \beta_\chi\tan\lambda)}. \tag{17}$$

The GH shift, in the presence of a scalar potential, is chirality dependent

$$\Delta_{\rm GH} = \frac{\hbar v_F}{E}\frac{\tilde{\kappa}^2(1-\tan^2\lambda) + 2\epsilon\chi\tilde{\kappa}\tan\lambda + \epsilon\sec^2\lambda\cos^2\bar{\theta}}{\tilde{\kappa}\sin\bar{\theta}\cos\bar{\theta}[1 - \epsilon + 2\tilde{\kappa}\chi\tan\lambda + (1+\epsilon)\tan^2\lambda]}, \tag{18}$$

where $\sin\theta_c \equiv -\epsilon = V_0/E - 1$ as defined before and $\tilde{\kappa} = \sqrt{\sin^2\bar{\theta} - \sin^2\theta_c} = \sqrt{\bar{k}_y^2 - (E - V_0)^2}/E = \kappa/E$ for $\bar{k}_z = 0$.

The IF shift, on the other hand, is insensitive to the scalar potential and retains its form as in Eq. (12), i.e.,

$$\Delta_{\rm IF} = -\frac{\hbar v_F}{E}\frac{\chi}{\tan\bar{\theta}}, \tag{19}$$

reflecting topological robustness against such type of potential. In the limit $\lambda \to 0$, we retrieve the clean results of Eq. (12).

At any finite strength of the scalar potential λ, the GH shift is evidently valley dependent and from the expression of the reflection phase ϕ_r in Eq. (17), $\lambda = n\pi$ (n integers) has the same effect as $\lambda = 0$ (clean case). Figures 2(a) and 2(b) show the functional dependence of $\Delta_{\rm GH}$ on the incident angle θ at various values of λ. Here we fix $V_0/E = 1.5$ which, in turn, gives a critical angle $\theta_c = 30^\circ$ below which total reflection does not occur. The main features of Figs. 2(a) and 2(b) are

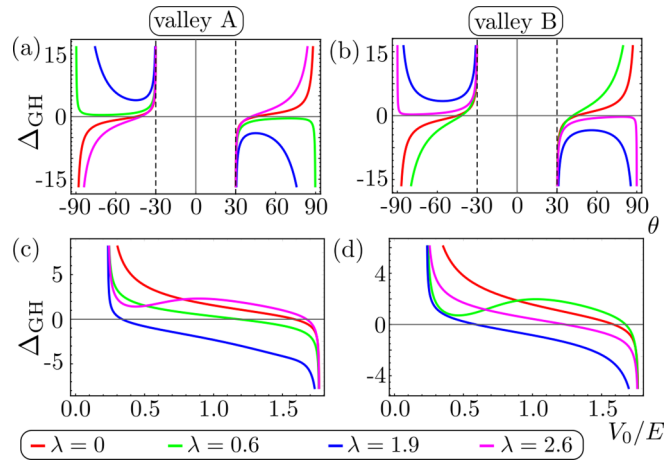

FIG. 2. Scalar potential: The valley-dependent GH shift (measured with respect to the length scale $\hbar v_F/E$) as a function of the incident angle θ for $V_0/E = 1.5$ ($E = 1$) for valley A in (a) and valley B in (b) at different strengths (λ) of the scalar surface potential. The critical angle $\theta_c = 30^\circ$ below which no total reflection takes place. The valley-dependent GH shift as a function of V_0/E for an incident angle $\theta = 50^\circ$ for valley A in (c) and valley B in (d). The clean case corresponds to $\lambda = 0$ (red). The other representative values of the scalar potential considered are $\lambda = 0.6$ (green), $\lambda = 1.9$ (blue), and $\lambda = 2.6$ (magenta).

highlighted below which are distinct for different chiralities (also referred to as valleys).

Valley A ($\chi = +1$): For $0 \leqslant \lambda < \lambda_1$ where $\lambda_1 = \pi/6$, $\Delta_{\rm GH}$ for valley A behaves qualitatively similar to the clean case, however, the value of θ at which its changes the sign, denoted $\theta^{*(+)}$, is λ dependent. We find $\theta^{*(+)} = \sin^{-1}\sqrt{\alpha_+^2 + 1/4}$, where

$$\alpha_+ = \frac{2\tan\lambda + \sqrt{\left[6\cos(2\lambda) - \frac{1}{2}\cos(4\lambda) + \frac{7}{2}\right]\sec^4(\lambda)}}{8 - 2\sec^2\lambda}. \tag{20}$$

In the aforementioned range, $\theta^{*(+)}$ gradually moves from 45° (at $\lambda = 0$) to 90° (at $\lambda = \lambda_1$) monotonically. The numerator in Eq. (18) for valley A changes sign at $\bar{\theta} = 90°$ across $\lambda = \lambda_1$, by virtue of which, for $\lambda_1 \leqslant \lambda \leqslant \lambda_2$ where $\lambda_2 = 2\pi/3$, $\Delta_{\rm GH}$ for valley A remains finite irrespective of the incident angle θ, i.e., $\theta^{*(+)}$ does not exist. The numerator for valley A changes sign again at $\bar{\theta} = 90°$ across $\lambda = \lambda_2$. As a result, for $\lambda_2 < \lambda \leqslant \pi$, $\theta^{*(+)}$ decreases from 90° (at $\lambda = \lambda_2$) to 45° (at $\lambda = \pi$), however not monotonically (it obtains a minimum somewhere before $\lambda = \pi$).

Valley B ($\chi = -1$): For $0 \leqslant \lambda < \lambda_3$ where $\lambda_3 = \pi/3$, $\Delta_{\rm GH}$ for valley B behaves qualitatively similar to the clean case, however, the value of θ at which its changes the sign, denoted $\theta^{*(-)}$, is λ dependent. We find $\theta^{*(-)} = \sin^{-1}\sqrt{\alpha_-^2 + 1/4}$, where

$$\alpha_- = \frac{-2\tan\lambda + \sqrt{\left[6\cos(2\lambda) - \frac{1}{2}\cos(4\lambda) + \frac{7}{2}\right]\sec^4(\lambda)}}{8 - 2\sec^2\lambda}. \tag{21}$$

In the aforementioned range, $\theta^{*(-)}$ increase from 45° (at $\lambda = 0$) to 90° (at $\lambda = \lambda_3$) but nonmonotonically (it attains a minimum somewhere in-between). The numerator in Eq. (18) for valley B changes sign at $\bar{\theta} = 90°$ across $\lambda = \lambda_3$, by virtue of which, for $\lambda_3 \leqslant \lambda \leqslant \lambda_4$ where $\lambda_4 = 5\pi/6$, $\Delta_{\rm GH}$ for valley B remains finite irrespective of the incident angle θ, i.e., $\theta^{*(-)}$ does not exist, just like valley A. The numerator for valley B changes sign again at $\bar{\theta} = 90°$ across $\lambda = \lambda_4$. Consequently, for $\lambda_4 < \lambda \leqslant \pi$, $\theta^{*(-)}$ decreases monotonically from 90° (at $\lambda = \lambda_4$) to 45° (at $\lambda = \pi$).

In summary, a notable aspect, which gains prominence from the above analysis, is that the GH shift, in the presence of scalar surface potential, can behave in vastly different ways for the two valleys—it can vanish for one of the valleys for certain values of the strength of the potential while, at the same time, it remains finite for the other. Note the plots of $\Delta_{\rm GH}$ against θ for the two valleys overlap at the transition points $\lambda = \lambda_{1,2,3,4}$. Figures 2(c) and 2(d) display the behavior of $\Delta_{\rm GH}$ against the ratio of the barrier height to the incident energy V_0/E which also feature a strong valley dependence in the presence of a scalar surface potential, namely, the values of V_0/E at which the GH shift vanishes, depends on the chirality, unlike the clean case. As the IF is not influenced by the scalar potential, we do not show its parametric dependence which is already discussed in Ref. [50]. In all the plots of the shifts (i.e., Fig. 2 to Fig. 7), the shift parameter Δ is measured with respect to the characteristic length scale $\hbar v_F/E$. In a typical Weyl system (such as the compound $Co_3Sn_2S_2$), Weyl nodes are realized around $E \sim 60$ meV while the Fermi velocity $v_F \sim 2 \times 10^6$ m/s. That provides an estimate of this length scale to be ∼22 nm. The departure due to the various types of surface potentials, discussed in this article, from the pristine results should therefore be measurable in the exiting mesoscopic setups.

B. Magnetic potential

For a magnetic impurity present all over the interface with field orientation $\vec{\mathbf{B}} = (B_x, B_y, B_z)$, the transfer matrix is

$$\mathcal{T} = e^{-i\sigma_x(\vec{\mathbf{B}}\cdot\vec{\sigma})} = e^{-iB_x}e^{B_y\sigma_z - B_z\sigma_y}. \tag{22}$$

The out-of-plane component B_x contributes merely as a phase factor and does not influence the shifts. For the remaining components, it is useful to introduce the parameters $B_\parallel = \sqrt{B_y^2 + B_z^2}$ and $\tan\Phi = B_z/B_y$. In terms of these parameters, the reflection phase is

$$\phi_r = -\theta - \frac{\pi}{2} + 2\tan^{-1}\zeta_B,$$

where

$$\zeta_B = \frac{\tilde{\eta}\cos\theta(b_B + \beta_\chi a_B)}{2\eta\chi(\beta_\chi + a_B) - \tilde{\eta}\sin\theta(b_B + \beta_\chi a_B)}, \tag{23}$$

with the parameters a_B and b_B defined as

$$a_B = \frac{\sin\Phi\tanh B_\parallel}{1 + \cos\Phi\tanh B_\parallel}; \quad b_B = \frac{1 - \cos\Phi\tanh B_\parallel}{1 + \cos\Phi\tanh B_\parallel}. \tag{24}$$

The corresponding shifts are given by

$$\Delta_{\rm GH} = \frac{\hbar v_F}{E}\frac{1}{\tilde{\kappa}\cos\bar{\theta}}\frac{\mathcal{N}_{\rm GH}}{\mathcal{D}}; \quad \Delta_{\rm IF} = \frac{\hbar v_F}{E}\frac{2\cos\bar{\theta}}{\mathcal{D}}\mathcal{N}_{\rm IF}, \tag{25}$$

where

$$\begin{aligned}
\mathcal{N}_{\rm GH} &= \tilde{\kappa}^2\left(b_B^2 + 1 - 2a_B^2\right) + \tilde{\kappa}\left(1 - b_B^2\right)\sin\bar{\theta} \\
&\quad + 2\epsilon\left[\chi\tilde{\kappa}a_B(1 - b_B) - \left(a_B^2 - b_B\right)\cos^2\bar{\theta}\right], \\
\mathcal{N}_{\rm IF} &= a_B(1 + b_B)\sin\bar{\theta} + a_B\tilde{\kappa}(1 - b_B) \\
&\quad + \chi\left[\left(a_B^2 + b_B\right)\epsilon + a_B^2 - b_B\right], \\
\mathcal{D} &= \left\{(\sin\bar{\theta} + \tilde{\kappa})\left(1 + a_B^2 - 2\chi a_B\sin\bar{\theta}\right)\right. \\
&\quad + (\sin\bar{\theta} - \tilde{\kappa})\left(a_B^2 + b_B^2 - 2a_Bb_B\chi\sin\bar{\theta}\right) \\
&\quad \left. + 2\epsilon\left[a_B\chi(1 + b_B) - a_B^2\sin\bar{\theta} - b_B\sin\bar{\theta}\right]\right\}.
\end{aligned} \tag{26}$$

Eq. (25) matches with the clean results in the limit $B_\parallel \to 0$.

Figure 3 displays the behavior of the GH shift $\Delta_{\rm GH}$ in the presence of magnetic surface potential at various values of the in-plane strength $B_\parallel$ and the orientation of the magnetic field characterized by the angle Φ defined previously. In Figs. 3(a)–3(d) $B_\parallel$ is being varied while keeping the orientation Φ fixed to $\pi/10$. In Figs. 3(e)–3(h) $B_\parallel = 1$ while the orientation Φ is being varied. The out-of-plane component has no effect on the shifts and is taken to be zero. In Figs. 3(a) and 3(b) $\Delta_{\rm GH}$ is plotted against the incident angle θ for the two different valleys, given $V_0/E = 1.5$. Evidently, $\Delta_{\rm GH}$ is no more an odd function of θ unlike the clean or the scalar case. The distinctive behavior of the two valleys is prominent that can be explained in the same way as the scalar potential. In Figs. 3(c)

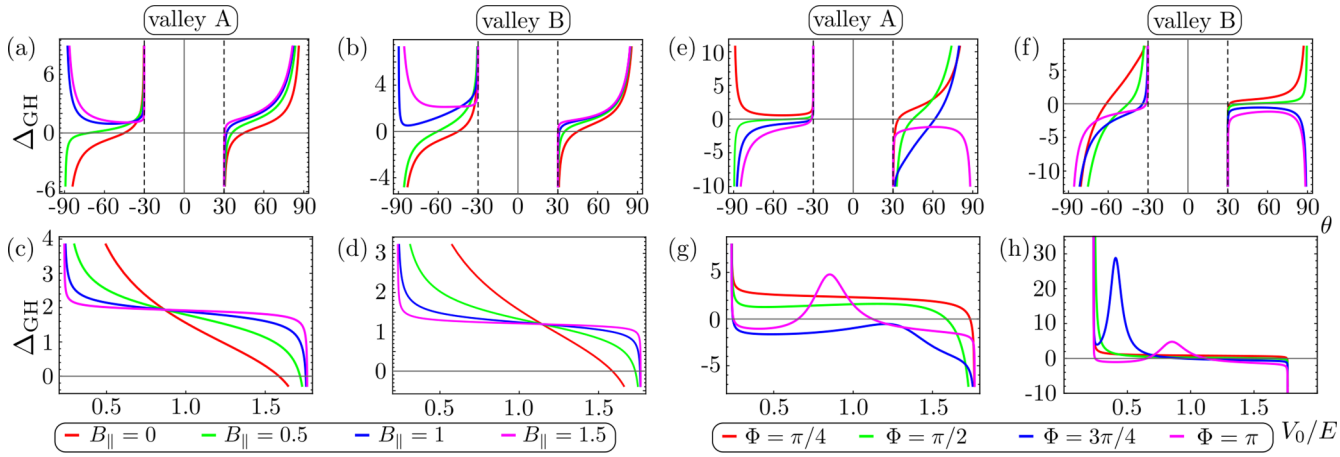

FIG. 3. Magnetic potential: The valley-dependent GH shift (measured with respect to the length scale $\hbar v_F/E$) as a function of the incident angle θ for $V_0/E = 1.5$ ($E = 1$) for valley A in (a) and valley B in (b) at different strengths of the in-plane magnetic field $B_\parallel$ keeping the orientation $\Phi = \pi/10$ and again for valley A in (e) and valley B in (f) at different orientations of the in-plane magnetic field Φ keeping the strength $B_\parallel = 1$. The critical angle $\theta_c = 30^\circ$ as before. The valley-dependent GH shift is plotted as a function of V_0/E with an incident angle $\theta = 50^\circ$ for valley A in (c) and valley B in (d) varying $B_\parallel$ which shows a plateaulike behavior as $B_\parallel$ is increased. The same varying Φ is shown in (g) for valley A and (h) for valley B which features a peak for certain values of the orientation which are distinct for different valleys. The clean case corresponds to $B_\parallel = 0$ (red) in (a)–(d) and the other parameter values are shown in different colors.

and 3(d) Δ_{GH} is plotted against V_0/E which, for both valleys, features a plateaulike behavior as $B_\parallel$ is increased. When the orientation Φ is varied, Δ_{GH} plotted against θ as in Figs. 3(e) and 3(f) behaves in a qualitatively similar way to Figs. 3(a) and 3(b), however, its variation against V_0/E is observed to develop conspicuous peaks for certain orientations whose height can differ in order of magnitudes between the two valleys as shown in Figs. 3(g) and 3(h).

The behavior of the IF shift in the presence of the magnetic surface potential is quite remarkable as shown in Fig. 4. Similar to Fig. 3, the variation with respect to $B_\parallel$ keeping Φ fixed is displayed in Figs. 4(a)–4(d) while the opposite is shown in Figs. 4(e)–4(h). Note that at any finite $B_\parallel$, the IF shift is defined only for $|\theta| > \theta_c$ where the total reflection takes place because of the parameter $\tilde{\kappa}$, unlike the clean case. For the clean case, this parameter in absent in the expression of Δ_{IF} as in Eq. (12). Besides the difference in magnitude, Δ_{IF} as a function of θ can have the same sign for the two valleys depending on the values of $B_\parallel$ when it is gradually increased. In Figs. 4(a) and 4(b), such a behavior is observed for $B_\parallel = 1.5$. Furthermore, from Eq. (25|), Δ_{IF} can change sign for $\chi = +1$ and vanishes at a specific value of ϵ or equiv-

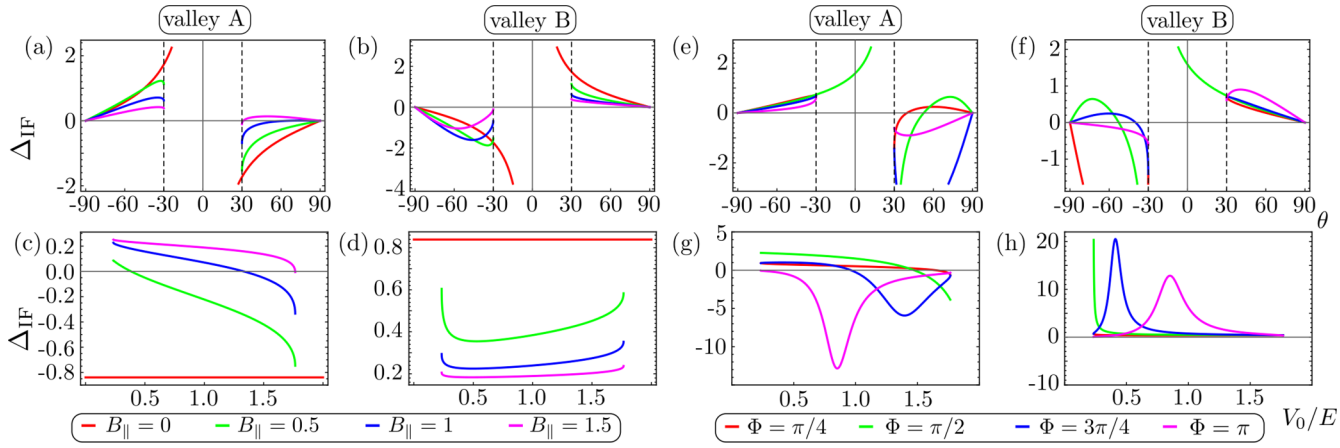

FIG. 4. Magnetic potential: The valley-dependent IF shift (measured with respect to the length scale $\hbar v_F/E$) as a function of the incident angle θ for $V_0/E = 1.5$ ($E = 1$) for valley A in (a) and valley B in (b) at different strengths of the in-plane magnetic field $B_\parallel$ keeping the orientation $\Phi = \pi/10$ and again for valley A in (e) and valley B in (f) at different orientations of the in-plane magnetic field Φ keeping the strength $B_\parallel = 1$. The critical angle $\theta_c = 30^\circ$ as before. The IF shift is plotted as a function of V_0/E with an incident angle $\theta = 50^\circ$ for valley A in (c) and valley B in (d) varying $B_\parallel$. A vanishing IF shift at this incidence is observed in the presence of a finite $B_\parallel$ which is specific to only one of the valleys (namely, A). The same varying Φ is shown in (g) for valley A and (h) for valley B which displays a peak for certain values of the orientation which are distinct for different valleys. The clean case corresponds to $B_\parallel = 0$ (red) in (a)–(d) and the other parameter values are shown in different colors.

alently V_0/E that depends on $B_\parallel$ and Φ. This is not the case for the other valley [see Figs. 4(c) and 4(d)]. In the clean case, i.e., for $B_\parallel = 0$, the factor containing ϵ drops off which results in $\Delta_{\rm IF}$ being independent of V_0/E with the chirality χ appearing as a prefactor. Thus, magnetic surface potential can lead to a vanishing IF shift for a specific valley ($\chi = +1$) at an incident angle $\theta_c < \theta < \pi/2$ while not having any such effect on the other. Upon varying the orientation Φ as in Figs. 4(e) and 4(f), for both valleys, the behavior appears similar to varying $B_\parallel$. In addition, when plotted against V_0/E, $\Delta_{\rm IF}$ exhibits a peak, similar to $\Delta_{\rm GH}$, for certain values of Φ as shown in Figs. 4(g) and 4(h) for $B_\parallel = 1$.

C. Rashba spin-orbit potential

For surface potentials resulting from Rashba type spin-orbit coupling $\mathcal{V} = \alpha_R(k_y\sigma_z - k_z\sigma_y)$, the transfer matrix is given as

$$\mathcal{T} = e^{-i\alpha_R\sigma_x(k_y\sigma_z - k_z\sigma_y)} = e^{-\alpha_R(k_z\sigma_z + k_y\sigma_y)} \tag{27}$$

and the reflection phase, in this case, ϕ_r turns out to be

$$\phi_r = -\theta - \frac{\pi}{2} + 2\tan^{-1}\zeta_R,$$

where

$$\zeta_R = \frac{\tilde{\eta}\cos\theta(1+\beta_\chi a_R)}{2\eta\chi(\beta_\chi b_R + a_R) - \tilde{\eta}\sin\theta(1+\beta_\chi a_R)}, \tag{28}$$

with the parameters a_R and b_R defined as

$$a_R = \frac{\cos\varphi\tanh(\alpha_R k_\parallel)}{1+\sin\varphi\tanh(\alpha_R k_\parallel)}; \quad b_R = \frac{1-\sin\varphi\tanh(\alpha_R k_\parallel)}{1+\sin\varphi\tanh(\alpha_R k_\parallel)}. \tag{29}$$

Here $k_\parallel = \sqrt{k_y^2 + k_z^2}$ and $\tan\varphi = k_z/k_y$.

Note the expression of ζ_R can be obtained from that of ζ_B by identifying $B_y \leftrightarrow -\alpha_R k_z$ and $B_z \leftrightarrow \alpha_R k_y$, or equivalently, $B_\parallel \leftrightarrow \alpha_R k_\parallel$ and $\Phi \leftrightarrow \pi/2 + \varphi$, which, in turn, identifies $a_B/b_B \leftrightarrow a_R$ and $b_B^{-1} \leftrightarrow b_R$. This readily yields Eq. (28) from Eq. (23). However, the results for the shifts that follow are significantly different from the magnetic impurity case since a_R and b_R are momentum-dependent parameters unlike a_B and b_B. This has distinct effects on the two shifts when we adopt a reference by setting $\bar{k}_z = 0$.

In detail, in this setting, the Rashba type surface potential appears to have no effect on the IF shift, i.e.,

$$\Delta_{\rm IF} = -\frac{\hbar v_F}{E}\frac{\chi}{\tan\bar{\theta}}, \tag{30}$$

same as the clean case. The chirality-dependent GH shift, however, is modified and given by

$$\Delta_{\rm GH} = \frac{\hbar v_F}{E}\frac{1}{\tilde{\kappa}\cos\bar{\theta}}\frac{\mathcal{N}_{\rm R}}{\mathcal{D}_{\rm R}}, \tag{31}$$

where

$$\begin{aligned}\mathcal{N}_{\rm R} &= (\tilde{\kappa}^2 + \epsilon\cos^2\bar{\theta} - 2\chi\alpha_R E\tilde{\kappa}^2\cos^2\bar{\theta})\mathrm{sech}^2(\alpha_R E\sin\bar{\theta}),\\ \mathcal{D}_{\rm R} &= \sin\bar{\theta}(1-\epsilon)[1+\tanh^2(\alpha_R E\sin\bar{\theta})]\\ &\quad + 2\chi\tanh(\alpha_R E\sin\bar{\theta})(\epsilon - \sin^2\bar{\theta}).\end{aligned} \tag{32}$$

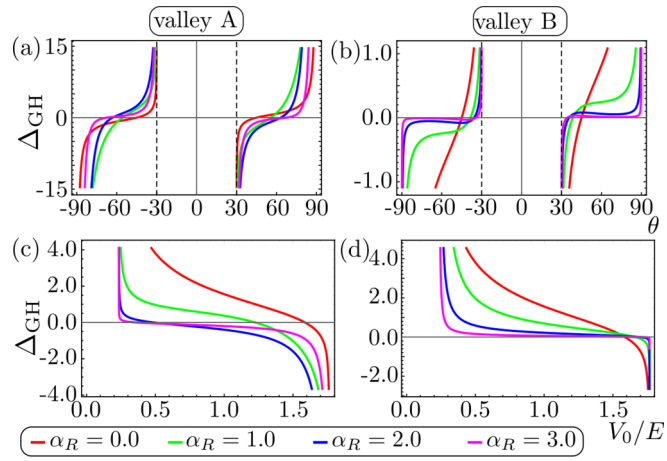

FIG. 5. Rashba potential: The valley-dependent GH shift (measured with respect to the length scale $\hbar v_F/E$) as a function of the incident angle θ for $V_0/E = 1.5$ ($E = 1$) for valley A in (a) and valley B in (b) at different strengths (α_R) of the Rashba spin-orbit potential. The same as a function of V_0/E for an incident angle $\theta = 50^\circ$ for valley A in (c) and valley B in (d). The clean case corresponds to $\alpha_R = 0$ (red).

It is straightforward to show that $\mathcal{N}_{\rm R}$ and $\mathcal{D}_{\rm R}$ approach their corresponding clean values in the limit $\alpha_R \to 0$. The general case for $\bar{k}_z \neq 0$ is discussed in Appendix B which indeed affects the IF shift.

The influence of Rashba-type surface potential on the shifts is depicted in Fig. 5. The GH shift behaves qualitatively very similar to the clean case in the sense that it is odd in θ and for all values of α_R below $\alpha_R \sim 10$ (beyond this, $\Delta_{\rm GH} \sim 10^{-5}$ and gets further suppressed with increasing α_R), there exists a θ^* at which the shift vanishes (and across which it changes sign) as can be seen in Figs. 5(a) and 5(b) for both valleys. The same comparison holds for the plots of $\Delta_{\rm GH}$ vs V_0/E [Figs. 5(c) and 5(d)] except that at large values of α_R, the GH shift plateaus over the entire range of V_0/E for both valleys. Furthermore, as shown above, the IF shift is not affected, and so we do not provide any parametric plot of $\Delta_{\rm IF}$ for this case.

D. Dresselhaus spin-orbit potential

For surface potentials that arise from Dresselhaus type spin-orbit coupling $\mathcal{V} = \alpha_D(k_y\sigma_y - k_z\sigma_z)$, the transfer matrix is given by

$$\mathcal{T} = e^{-i\alpha_D\sigma_x(k_y\sigma_y - k_z\sigma_z)} = e^{\alpha_D(k_z\sigma_y + k_y\sigma_z)}, \tag{33}$$

which results in a reflection phase

$$\phi_r = -\theta - \frac{\pi}{2} + 2\tan^{-1}\zeta_D,$$

where

$$\zeta_D = \frac{\tilde{\eta}\cos\theta(b_D - \beta_\chi a_D)}{2\eta\chi(\beta_\chi - a_D) - \tilde{\eta}\sin\theta(b_D - \beta_\chi a_D)}, \tag{34}$$

with the parameters a_D and b_D defined as

$$a_D = \frac{\sin\varphi\tanh(\alpha_D k_\parallel)}{1+\cos\varphi\tanh(\alpha_D k_\parallel)}; \quad b_D = \frac{1-\cos\varphi\tanh(\alpha_D k_\parallel)}{1+\cos\varphi\tanh(\alpha_D k_\parallel)}. \tag{35}$$

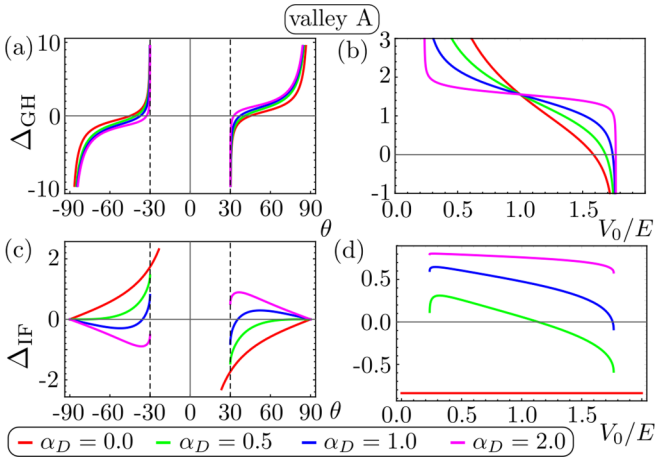

FIG. 6. Dresselhaus potential: The GH shift (measured with respect to the length scale $\hbar v_F/E$) as a function of the incident angle θ for $V_0/E = 1.5$ ($E = 1$) in (a) and the same as a function of V_0/E with $\theta = 50^\circ$ in (b) for valley A at different strengths (α_D) of the Dresselhaus spin-orbit potential. The IF shift under the same setup in (c) and (d). Note here Δ_{GH} is valley independent while $\Delta_{IF} \propto \chi$ like the clean case ($\alpha_D = 0$).

Here a straightforward identification $a_B \leftrightarrow -a_D$ and $b_B \leftrightarrow b_D$ (by virtue of $B_\parallel \leftrightarrow \alpha_D k_\parallel$ and $\Phi \leftrightarrow 2\pi - \varphi$) would yield Eq. (34) from Eq. (23).

Following analogous calculations as the Rashba case above, we obtain the shifts as

$$\Delta_{GH} = \frac{\hbar v_F}{E}\frac{1}{\tilde{\kappa}\cos\bar{\theta}}\frac{\mathcal{N}_D^{(GH)}}{\mathcal{D}_D}; \quad \Delta_{IF} = -\frac{\hbar v_F}{E}\frac{\chi}{\tan\bar{\theta}}\frac{\mathcal{N}_D^{(IF)}}{\mathcal{D}_D}, \tag{36}$$

where

$$\begin{aligned}\mathcal{N}_D^{(IF)} &= (1-\epsilon)[1-\tanh^2(\alpha_D E\sin\bar{\theta})]\sin\bar{\theta} \\ &\quad - 2\tilde{\kappa}\tanh(\alpha_D E\sin\bar{\theta}) - 2\tanh^2(\alpha_D E\sin\bar{\theta})\sin\bar{\theta}, \\ \mathcal{N}_D^{(GH)} &= (\tilde{\kappa}^2 + \epsilon\cos^2\bar{\theta} + 2\alpha_D\epsilon\tilde{\kappa}E\cos^2\bar{\theta}) \\ &\quad + 2\tanh(\alpha_D E\sin\bar{\theta})\tilde{\kappa}\sin\bar{\theta} + \tanh^2(\alpha_D E\sin\bar{\theta}) \\ &\quad \times [\tilde{\kappa}^2 - \epsilon\cos^2\bar{\theta} - 2\alpha_D\epsilon\tilde{\kappa}E\cos^2\bar{\theta}],\end{aligned} \tag{37}$$

and

$$\begin{aligned}\mathcal{D}_D &= \sin\bar{\theta}(1-\epsilon) + 2\tilde{\kappa}\tanh(\alpha_D E\sin\bar{\theta}) \\ &\quad + \tanh^2(\alpha_D E\sin\bar{\theta})\sin\bar{\theta}(1+\epsilon).\end{aligned} \tag{38}$$

Again, the clean results are readily obtained in the limit $\alpha_D \to 0$.

The Dresselhaus-type surface potential has quite a few exotic effects on both shifts. First, from the above expressions, Δ_{GH} is chirality independent and odd in θ while Δ_{IF} carries the same chirality dependence as the clean case, i.e., $\Delta_{IF} \propto \chi$. This is reflected in Fig. 6. In Fig. 6(a) Δ_{GH} is plotted against θ keeping $V_0/E = 1.5$. Similar to the other potentials, a θ^* exists at which Δ_{GH} vanishes in a given range of α_D beyond which $|\Delta_{GH}|$ remains finite. In Fig. 6(b) Δ_{GH} is plotted against V_0/E keeping $\theta = 50^\circ$. We note while at small values of α_D, the behavior of Δ_{GH} looks qualitatively similar to the clean case, as α_D is gradually increased, the plateauing effect starts dominating, and eventually, at very large values of α_D, Δ_{GH} saturates at a value that increases with θ.

For the IF shift we find that the Dresselhaus type surface potential can interestingly lead to phenomena like valley inversion as seen in Fig. 6(c) in the following manner. Let us denote the value of θ at which the IF shift vanishes by θ^*_{IF}. For the clean case, $|\theta^*_{IF}| = \pi/2$. When α_D is increased, there appears another θ^*_{IF} such that $|\theta^*_{IF}| < \pi/2$ which gradually approaches θ_c as α_D approaches

$$\alpha_D^* = \frac{1}{E\sin\theta_c}\tanh^{-1}\frac{V_0}{V_0+2}. \tag{39}$$

If α_D is increased further beyond this value, a valley inversion takes place as Δ_{IF} changes sign across $\alpha_D = \alpha_D^*$. Similar phenomenon is also observed in the plot of Δ_{IF} against V_0/E as in Fig. 6(d) where the valley inversion manifests as reordering of the curves of Δ_{IF} against V_0/E at different values of θ as α_D is increased and consequently, $\Delta_{IF}(\theta) \to -\Delta_{IF}(\theta)$.

V. DISCUSSION

In this article we revisited the phenomena of GH and IF shifts, the lateral shifts of an incident beam upon total reflection, in a Weyl semimetal system to discuss the effects of surface potentials on these shifts which could be probed in real materials. Earlier these shifts were studied for a clean Weyl surface and argued that the IF shift is topological in nature, namely, it is chirality dependent and so can be exploited in experiments to characterize Weyl systems. The GH shift in Weyl semimetals, on the other hand, does not have such a feature. However, as we reveal in this article, this is not entirely true when the concerned surface harbors various kinds of surface potentials as is the case in real materials exhibiting Weyl nodes. Among the key observations, the presence of any type of surface potential renders the GH shift strongly chirality dependent. In fact, strong scalar or magnetic potential can yield a situation in which the GH shift remains finite irrespective of the incident angle for the allowed values of the magnitude of the chemical potential barrier (V_0) that distinguishes the surface. For other types of surface potentials such as the Rashba or Dresselhaus type, the GH shift shows a conspicuous departure from the clean results. In the case of magnetic impurities, when plotted as a function of the barrier height V_0, strong surface potentials give rise to a plateauing effect in the GH shift and sometimes, pronounced cusps at specific values of V_0. These effects can be particularly useful in probing magnetic Weyl systems that have recently nucleated experimental activities.

For the IF shift, the scalar surface potentials turn out to have no effect, however, a statement is in order. This is specific to the reference used which is $\bar{k}_z = 0$, otherwise, a

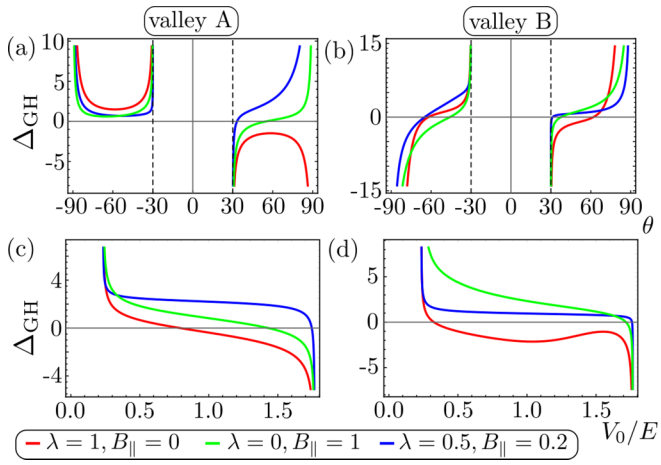

FIG. 7. Combination of scalar and Zeeman potential: GH shift (measured with respect to the length scale $\hbar v_F/E$) as a function of the incident angle θ for $V_0/E = 1.5$ for valley A in (a) and valley B in (b) at different strengths of the scalar surface potential (λ) and magnetic potential ($B_\parallel$). The same as a function of V_0/E at $\theta = 50^\circ$ for valley A in (c) and valley B in (d). The combinations of λ and $B_\parallel$ are specified in different colors as $\lambda = 1, B_\parallel = 0$ in red, $\lambda = 0, B_\parallel = 1$ in green, $\lambda = 0.5, B_\parallel = 0.2$ in blue.

finite contribution to the IF shift due to a scalar potential can arise as discussed in Appendix A. On the other hand, even in this simple setting, the other kinds of surface potentials leave remarkable signatures compared to the clean case similar to when intervalley scattering takes place. Most promising are the magnetic and Dresselhaus-type impurities, in the presence of which, the IF shift, which otherwise is independent of V_0 and changes sign between the two valleys for the clean case, develops a strong valley asymmetry beyond a simple sign inversion and also a parametric dependence on V_0 such that it can vanish at certain values of V_0 depending on the incident angle θ. Similarly, in distinction to the clean case where the IF shift vanishes only at $\theta = \pm\pi/2$, the impurities can enforce intermediate values of $0 < |\theta| < \pi/2$ at which the IF shift is nullified and that too can be valley dependent. This can potentially mask the IF shift to be identified as a topological effect in realistic Weyl systems as their surfaces would typically host various impurities even including a mixed nature.

To investigate the effects of such mixed impurities, we study the case where the surface potential includes both the scalar and magnetic contributions as $\mathcal{V} = \lambda + \mathbf{B}\cdot\sigma$. The results are summarized in Fig. 7. While the IF shift (not shown) is dictated by the magnetic contribution, the GH shift is affected by both. In fact, as revealed by Fig. 7, the plateauing effect is stronger when both types of surface potentials are present with moderate strengths, compared to their individual influences at higher strengths. If the two impurities form distinct domains on the surface, we expect the resultant shifts to be a weighted average of the individual shifts as $\langle\Delta\rangle = w\langle\Delta_1\rangle + (1-w)\langle\Delta_2\rangle$ where the two kinds of impurities are denoted by 1 and 2 and $\langle\cdots\rangle$ implies ensemble averaging that includes the impurities with probabilities w and $(1-w)$, respectively. This extends to multiple types of impurities as well.

In summary, our work extends the phenomena of GH and IF shift in Weyl semimetals beyond a clean surface and accommodates surface potentials to unveil novel features of the shifts. Our observations would provide useful guidance to experiments that are tuned to characterize Weyl systems based on such phenomena that have already found potential relevance in device applications engaging other electronic systems. Studying similar effects on other transport properties of Weyl semimetals will be addressed elsewhere.

ACKNOWLEDGMENTS

N.K.D. and K.R. gratefully acknowledge the useful discussion with Qing-Dong Jiang and Sourin Das and thank them for critically reviewing the manuscript. K.R. also thanks the sponsorship, in part, by the Swedish Research Council.

APPENDIX A: IF SHIFT DUE TO THE SCALAR POTENTIAL FOR $\bar{k}_z \neq 0$

Here we present the expression of the IF shift for $\bar{k}_z \neq 0$ in the presence of a scalar potential that reads

$$\begin{aligned}\Delta_{\rm IF} = -\frac{2}{G^2}[&-2\eta\tilde{\eta}\chi\cos\bar{\theta}(1+\tan^2\lambda)\beta_\chi^{(1)}\\ &+2\chi\cos\bar{\theta}(1-\beta_\chi\tan\lambda)(\beta_\chi+\tan\lambda)(\eta\tilde{\eta}^{(1)}-\tilde{\eta}\eta^{(1)})]\\ &+\theta^{(1)}\Bigg[1+\frac{\tilde{\eta}^2-4\eta^2}{\tilde{\eta}^2+4\eta^2}-\frac{2\tilde{\eta}^2(1-\beta_\chi\tan\lambda)^2}{G^2}\\ &+\frac{2\chi\eta\tilde{\eta}\sin\bar{\theta}(\beta_\chi+\tan\lambda)(1-\beta_\chi\tan\lambda)}{G^2}\Bigg],\end{aligned} \tag{A1}$$

where

$$\beta^{(1)} = \frac{\partial\beta_\chi/\partial k_z|_{\bar{k}_z=0}}{\left[1+\frac{\chi\bar{k}_z}{(E-V_0)}\right]^2}\left[1-\frac{\chi\bar{k}_z(E-V_0)}{\kappa(\bar{k}_y+\kappa)}\left(1+\frac{\chi\bar{k}_z}{(E-V_0)}\right)\right],$$

$$\eta^{(1)} = \frac{1}{\eta}\frac{\partial\eta/\partial k_z|_{\bar{k}_z=0}}{\left[1+\frac{\bar{k}_z}{E}\right]^2},$$

$$\tilde{\eta}^{(1)} = 2(1+\chi)\eta\eta^{(1)},$$

$$\theta^{(1)} = \frac{\bar{k}_y}{\sqrt{E^2-\bar{k}_y^2-\bar{k}_z^2}}\frac{\bar{k}_z}{(E^2-\bar{k}_z^2)},$$

$$\begin{aligned}G^2 = &\tilde{\eta}^2(1-\beta_\chi\tan\lambda)^2+4\eta^2(\beta_\chi+\tan\lambda)^2\\ &-4\eta\tilde{\eta}\chi\sin\bar{\theta}(\beta_\chi+\tan\lambda)(1-\beta_\chi\tan\lambda).\end{aligned} \tag{A2}$$

Note $\theta^{(1)}$ vanishes at $\bar{k}_z = 0$ and the term remaining in Eq. (A1) simplifies to Eq. (19) (without the prefactor $\hbar v_F/E$). Also the quantities $\beta_\chi, \eta, \tilde{\eta}$ in the above expressions are evaluated at $k_y = \bar{k}_y, k_z = \bar{k}_z$.

APPENDIX B: IF SHIFT DUE TO THE RASHBA-TYPE POTENTIAL FOR $\bar{k}_z \neq 0$

Here we present the expression of the IF shift for $\bar{k}_z \neq 0$ in the presence of a Rashba-type potential that reads

$$\begin{aligned}\Delta_{\mathrm{IF}} = &-\frac{2}{G_{\mathrm{R}}^2}\big[2\eta\tilde{\eta}\chi\cos\bar{\theta}\beta_\chi^{(1)}\big[a_R^2 - b_R\big] \\ &+ 2\chi\cos\bar{\theta}(1+\beta_\chi a_R)(a_R+\beta_\chi b_R)[\eta\tilde{\eta}^{(1)} - \tilde{\eta}\eta^{(1)}] \\ &+ 2\eta\cos\bar{\theta}\tilde{\eta}\chi\big[\beta_\chi^2 b_R - 1\big]a_R^{(1)} \\ &- 2\eta\chi\tilde{\eta}\cos\bar{\theta}\beta_\chi(1+\beta_\chi a_R)b_R^{(1)}\big] + \theta^{(1)}[\cdots], \end{aligned} \tag{B1}$$

where

$$\begin{aligned} a_R^{(1)} &= -\frac{\bar{k}_y}{\bar{k}_\parallel^2}\frac{\tanh(\alpha_R\bar{k}_\parallel)[\tanh(\alpha_R\bar{k}_\parallel)+\sin\bar{\varphi}]}{[\tanh(\alpha_R\bar{k}_\parallel)\sin\bar{\varphi}+1]^2} \\ &\quad + \frac{\bar{k}_z}{\bar{k}_\parallel}\frac{\alpha_R\,\mathrm{sech}^2(\alpha_R\bar{k}_\parallel)\cos\bar{\varphi}}{[\tanh(\alpha_R\bar{k}_\parallel)\sin\bar{\varphi}+1]^2}, \\ b_R^{(1)} &= -\frac{\bar{k}_y}{\bar{k}_\parallel^2}\frac{2\tanh(\alpha_R\bar{k}_\parallel)\cos\bar{\varphi}}{[\tanh(\alpha_R\bar{k}_\parallel)\sin\bar{\varphi}+1]^2} \\ &\quad - \frac{\bar{k}_z}{\bar{k}_\parallel}\frac{2\alpha_R\,\mathrm{sech}^2(\alpha_R\bar{k}_\parallel)\sin\bar{\varphi}}{[\tanh(\alpha_R\bar{k}_\parallel)\sin\bar{\varphi}+1]^2}, \\ G_{\mathrm{R}}^2 &= \tilde{\eta}^2(1+\beta_\chi a_R)^2 + 4\eta^2(a_R+\beta_\chi a_R)^2 \\ &\quad - 4\eta\tilde{\eta}\chi\sin\bar{\theta}(1+\beta_\chi a_R)(a_R+\beta_\chi a_R), \end{aligned} \tag{B2}$$

and $\bar{k}_\parallel = \sqrt{\bar{k}_y^2+\bar{k}_z^2}$, $\tan\bar{\varphi} = \bar{k}_z/\bar{k}_y$. Again it is straightforward to show that setting $\bar{k}_z = 0$ in Eq. (B1) reproduces the expression in Eq. (30) (without the prefactor $\hbar v_F/E$).

[1] F. Goos and H. Hänchen, Ann. Phys. **436**, 333 (1947).
[2] K. Artmann, Ann. Phys. **437**, 87 (1948).
[3] M. McGuirk and C. Carniglia, J. Opt. Soc. Am. **67**, 103 (1977).
[4] F. I. Fedorov, J. Optics **15**, 014002 (2013).
[5] H. Schilling, Ann. Phys. **471**, 122 (1965).
[6] C. Imbert, Phys. Rev. D **5**, 787 (1972).
[7] W. J. Wild and C. L. Giles, Phys. Rev. A **25**, 2099 (1982).
[8] F. Bretenaker, A. Le Floch, and L. Dutriaux, Phys. Rev. Lett. **68**, 931 (1992).
[9] E. Pfleghaar, A. Marseille, and A. Weis, Phys. Rev. Lett. **70**, 2281 (1993).
[10] O. Emile, T. Galstyan, A. Le Floch, and F. Bretenaker, Phys. Rev. Lett. **75**, 1511 (1995).
[11] C. Bonnet, D. Chauvat, O. Emile, F. Bretenaker, A. Le Floch, and L. Dutriaux, Opt. Lett. **26**, 666 (2001).
[12] P. R. Berman, Phys. Rev. E **66**, 067603 (2002).
[13] C.-F. Li, Phys. Rev. Lett. **91**, 133903 (2003).
[14] J. Fan, A. Dogariu, and L. Wang, Opt. Express **11**, 299 (2003).
[15] I. V. Shadrivov, A. A. Zharov, and Y. S. Kivshar, Appl. Phys. Lett. **83**, 2713 (2003).
[16] D. Felbacq, A. Moreau, and R. Smaâli, Opt. Lett. **28**, 1633 (2003).
[17] X. Yin, L. Hesselink, Z. Liu, N. Fang, and X. Zhang, Appl. Phys. Lett. **85**, 372 (2004).
[18] M. Merano, A. Aiello, M. Van Exter, E. Eliel, J. Woerdman *et al.*, Opt. Express **15**, 15928 (2007).
[19] C. W. J. Beenakker, R. A. Sepkhanov, A. R. Akhmerov, and J. Tworzydło, Phys. Rev. Lett. **102**, 146804 (2009).
[20] V.-O. de Haan, J. Plomp, T. M. Rekveldt, W. H. Kraan, A. A. van Well, R. M. Dalgliesh, and S. Langridge, Phys. Rev. Lett. **104**, 010401 (2010).
[21] A. Nieminen, A. Marini, and M. Ornigotti, J. Opt. **22**, 035601 (2020).
[22] L.-K. Shi and J. C. W. Song, Phys. Rev. B **100**, 201405(R) (2019).
[23] X. Chen, C.-F. Li, and Y. Ban, Phys. Rev. B **77**, 073307 (2008).
[24] S. C. Miller Jr. and N. Ashby, Phys. Rev. Lett. **29**, 740 (1972).
[25] D. Fradkin and R. Kashuba, Phys. Rev. D **9**, 2775 (1974).
[26] X. Chen, J.-W. Tao, and Y. Ban, Eur. Phys. J. B **79**, 203 (2011).
[27] M. Sharma and S. Ghosh, J. Phys.: Condens. Matter **23**, 055501 (2011).
[28] F. Zhai, Y. Ma, and K. Chang, New J. Phys. **13**, 083029 (2011).
[29] M. Cheng, Eur. Phys. J. B **85**, 89 (2012).
[30] Y. Wang, Y. Liu, and B. Wang, Phys. E **48**, 191 (2013).
[31] X. Chen, X.-J. Lu, Y. Ban, and C.-F. Li, J. Opt. **15**, 033001 (2013).
[32] Y. Wang, Y. Liu, and B. Wang, Phys. E **53**, 186 (2013).
[33] S. Grosche, M. Ornigotti, and A. Szameit, Opt. Express **23**, 30195 (2015).
[34] X. Zeng, M. Al-Amri, and M. S. Zubairy, Opt. Express **25**, 23579 (2017).
[35] W. Wu, W. Zhang, S. Chen, X. Ling, W. Shu, H. Luo, S. Wen, and X. Yin, Opt. Express **26**, 23705 (2018).
[36] A. Das and M. Pradhan, J. Opt. Soc. Am. B **38**, 387 (2021).
[37] Y. Fan, N.-H. Shen, F. Zhang, Z. Wei, H. Li, Q. Zhao, Q. Fu, P. Zhang, T. Koschny, and C. M. Soukoulis, Adv. Opt. Mater. **4**, 1824 (2016).
[38] Z. Zheng, F. Lu, L. Jiang, X. Jin, X. Dai, and Y. Xiang, Opt. Commun. **452**, 227 (2019).
[39] J.-Y. Liu, T.-J. Huang, L.-Z. Yin, F.-Y. Han, and P.-K. Liu, IEEE Photonics J. **12**, 2 (2020).
[40] Q. Zhang and K. Chan, Appl. Phys. Lett. **105**, 212408 (2014).
[41] Z. Wu, F. Zhai, F. M. Peeters, H. Q. Xu, and K. Chang, Phys. Rev. Lett. **106**, 176802 (2011).
[42] N. Peres, Rev. Mod. Phys. **82**, 2673 (2010).
[43] W. J. M. Kort-Kamp, N. A. Sinitsyn, and D. A. R. Dalvit, Phys. Rev. B **93**, 081410(R) (2016).
[44] A. Farmani, M. Miri, and M. H. Sheikhi, J. Opt. Soc. Am. B **34**, 1097 (2017).
[45] G. Xu, J. Sun, H. Mao, and T. Pan, Phys. Lett. A **381**, 2876 (2017).
[46] C. Luo, Z. Wang, X. Dai, and Y. Xiang, J. Opt. Soc. Am. B **35**, 2889 (2018).
[47] M. Zhu, J. Magn. Magn. Mater. **487**, 165319 (2019).
[48] W. J. M. Kort-Kamp, Phys. Rev. Lett. **119**, 147401 (2017).
[49] W. Wu, S. Chen, W. Xu, Z. Liu, R. Lou, L. Shen, H. Luo, S. Wen, and X. Yin, Photonics Res. **8**, B47 (2020).

[50] Q.-D. Jiang, H. Jiang, H. Liu, Q.-F. Sun, and X.-C. Xie, Phys. Rev. Lett. **115**, 156602 (2015).
[51] Q.-D. Jiang, H. Jiang, H. Liu, Q.-F. Sun, and X. C. Xie, Phys. Rev. B **93**, 195165 (2016).
[52] L. Wang and S.-K. Jian, Phys. Rev. B **96**, 115448 (2017).
[53] Y.-R. Hao, L. Wang, and D.-X. Yao, Phys. Rev. B **99**, 165406 (2019).
[54] G. Ye, W. Zhang, W. Wu, S. Chen, W. Shu, H. Luo, and S. Wen, Phys. Rev. A **99**, 023807 (2019).
[55] U. Chattopadhyay, L.-K. Shi, B. Zhang, J. C. W. Song, and Y. D. Chong, Phys. Rev. Lett. **122**, 066602 (2019).
[56] S. Liu, Y. Shou, X. Zhou, W. Cheng, and Z. Luo, Opt. Express **28**, 10783 (2020).
[57] P. Hosur and X. Qi, C. R. Phys. **14**, 857 (2013).
[58] M. Z. Hasan, S.-Y. Xu, I. Belopolski, and S.-M. Huang, Annu. Rev. Condens. Matter Phys. **8**, 289 (2017).
[59] F. Zhang, C. L. Kane, and E. J. Mele, Phys. Rev. B **86**, 081303(R) (2012).
[60] S. Roy and S. Das, Phys. Rev. B **93**, 085422 (2016).
[61] S. Roy, K. Roychowdhury, and S. Das, New J. Phys. **18**, 073038 (2016).
[62] D. Liu, A. Liang, E. Liu, Q. Xu, Y. Li, C. Chen, D. Pei, W. Shi, S. Mo, P. Dudin *et al.*, Science **365**, 1282 (2019).
[63] S.-M. Huang, S.-Y. Xu, I. Belopolski, C.-C. Lee, G. Chang, B. Wang, N. Alidoust, G. Bian, M. Neupane, A. Bansil *et al.*, Nat Commun. **6**, 7373 (2015).
[64] Z. Huang, D. P. Arovas, and A. V. Balatsky, New J. Phys. **15**, 123019 (2013).
[65] C. He, Phys. Lett. A **382**, 440 (2018).
[66] S. Pinon, V. Kaladzhyan, and C. Bena, Phys. Rev. B **101**, 115405 (2020).
[67] M. Calkin, D. Kiang, and Y. Nogami, Am. J. Phys. **55**, 737 (1987).
[68] R. Ilan, J. Cayssol, J. H. Bardarson, and J. E. Moore, Phys. Rev. Lett. **109**, 216602 (2012).
[69] E. Xypakis, J.-W. Rhim, J. H. Bardarson, and R. Ilan, Phys. Rev. B **101**, 045401 (2020).
[70] V. Adak, K. Roychowdhury, and S. Das, Phys. Rev. B **102**, 035423 (2020).